



## Research Paper

## A novel open-framework spheniscidite photocatalyst with excellent visible light photocatalytic activity: Silver sensitization effect and DFT study

Dandan Tang<sup>a,b,c</sup>, Jun Li<sup>a,b</sup>, Gaoke Zhang<sup>a,b,\*</sup><sup>a</sup> Hubei Key Laboratory of Mineral Resources Processing and Environment, School of Resources and Environmental Engineering, Wuhan University of Technology, 122 Luoshi Road, Wuhan 430070, China<sup>b</sup> State Key Laboratory of Silicate Materials for Architectures, Wuhan University of Technology, Wuhan 430070, China<sup>c</sup> School of Water Resources & Environmental Engineering, East China University of Technology, Nanchang 330013, China

## ARTICLE INFO

**Keywords:**  
 Spheniscidite  
 Silver modification  
 Visible light  
 Photocatalyst  
 DFT calculation

## ABSTRACT

We report a novel silver modified spheniscidite (SPH–Ag) visible light responsive photocatalyst with open-framework structure. The SPH–Ag photocatalyst was firstly synthesized by one step hydrothermal method. Meanwhile, the contribution of silver sensitization to the visible light photocatalytic property of SPH–Ag was confirmed by characterization results and DFT calculation.  $\text{Ag}^+$  is demonstrated to enter into the spheniscidite cavities and replace one  $\text{NH}_4^+$  per unit cell without destroying the structure. Noteworthy, compared to SPH, the pure phase SPH–Ag catalyst equipped with larger specific surface area, broader visible light response region, stronger oxidizing ability and lower recombination rate of electrons and holes. Meanwhile, the valence electrons are rearranged and the unoccupied  $\text{Ag} 5s$  orbital hybridizes with  $\text{Fe} 3d$  and  $\text{O} 2p$  orbitals at valance band, which greatly improves the SPH–Ag's ability of gaining electrons and the separation of photo generated charge carriers. As expected, the SPH–Ag catalyst exhibited enhanced photocatalytic activity for ARG degradation under visible light irradiation, which is mainly attributed to the generation of  $\text{h}^+$  and  $\cdot\text{O}_2^-$  species. Furthermore, its photocatalytic property was highly maintained as well as its structure and surface chemical properties after five recycles. This work may provide insight into the design of new-type Ag-based photocatalysts and their photocatalytic mechanism.

## 1. Introduction

The photocatalytic technology has attracted constant attention for its potential application for energy conversion and environment purification. In the last decades,  $\text{TiO}_2$  is the most popularly studied photocatalyst. However, its wide band gap has greatly limited its visible light utilization. Therefore, numerous efforts have been devoted to optimizing conventional photocatalysts [1–6] and exploring novel visible light responsive photocatalysts [7–14].

Open-framework materials are reported to have great potential applications for catalysis, sorption and separation processes [15]. In 1976,  $[\text{NH}_4]^+ [\text{Fe}_2(\text{OH})(\text{H}_2\text{O})(\text{PO}_4)_2] \cdot 2\text{H}_2\text{O}$  (spheniscidite) is reported as an ammonium rich leucophosphate by the IMA Commission on New Minerals and Mineral Names [16]. This three-dimensional iron phosphate mineral crystallizes in the monoclinic space group  $P2_1/n$ , which is consisted of  $\text{FeO}_6$  octahedra and  $\text{PO}_4$  tetrahedron networking [17]. The cavities of the framework are occupied by  $\text{NH}_4^+$  cations and water molecules [18]. Specifically,  $\text{NH}_4^+$  existed in the tunnels of the SPH is

capable of being replaced by other metal cations like  $\text{K}^+$  and  $\text{Li}^+$  [16,19]. Besides, literatures [15,20] reported that spheniscidite exhibits reversible dehydration, good adsorption ability and anti-ferromagnetism.

Up to now, reports on the application of spheniscidite are very limited. Redrup [19] and Reale [21] both found that spheniscidite has the potential for Li battery applications. However, no literatures on the application of spheniscidite as photocatalyst were published. Recently, Ag-containing catalysts have been widely investigated as catalysts [22–27]. The unique  $d^{10}$  electronic structure of silver cation is favorable for the formation and hybridization of semiconductor's valance band [28,29]. In particular, silver-containing catalysts like  $\text{AgX}$  ( $\text{X} = \text{Cl}, \text{Br}, \text{I}$ ),  $\text{Ag}_2\text{O}$ ,  $\text{Ag}_2\text{S}$ ,  $\text{Ag}_3\text{PO}_4$  and  $\text{Ag}_{10}\text{Si}_4\text{O}_{13}$  have been determined to show excellent photocatalytic activities [30,31]. Inspired by these studies, in this work, we designed and synthesized silver modified SPH (SPH–Ag) by a facial hydrothermal method, which was firstly applied as a visible light responsive photocatalyst. The preparation conditions like mole ratios of Fe/P/Ag, synthesis temperature, time and pH (amount of urea)

\* Corresponding author at: Hubei Key Laboratory of Mineral Resources Processing and Environment, School of Resources and Environmental Engineering, Wuhan University of Technology, 122 Luoshi Road, Wuhan 430070, China.

E-mail address: [gkzhang@whut.edu.cn](mailto:gkzhang@whut.edu.cn) (G. Zhang).

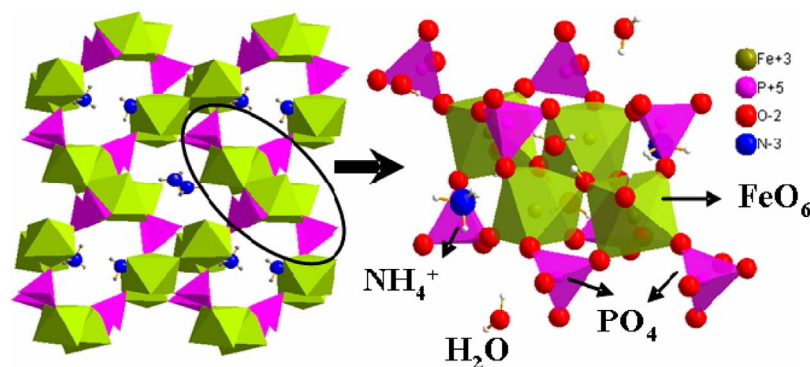


**Fig. 1.** The  $2 \times 2 \times 2$  structure and the basic building unit present in spheniscidite (note that water molecules and hydroxyl bonds are not shown in the left image).

were optimized. The crystal structure, morphology, surface chemical properties and electronic band structures of the obtained catalysts were studied by characterization technologies. Besides, the photocatalytic activities of the catalysts were evaluated by Acid Red G (ARG) degradation under simulated visible light irradiation. The existence form of silver and its modification mechanism in the SPH–Ag were discussed based on the experiment results and DFT calculation. Finally, the possible photocatalytic mechanism of ARG degradation over the SPH–Ag catalyst was proposed.

## 2. Materials and methods

### 2.1. Material synthesis

All chemicals utilized in this work are all of analytical reagent grade, which are used as purchased from Sinopharm Chemical Reagent Co. Ltd., China. The pure phase spheniscidite material (SPH) was prepared by a facial hydrothermal method. Typically, 0.6603 g of  $(\text{NH}_4)_2\text{HPO}_4$ , 1.0100 g of  $\text{Fe}(\text{NO}_3)_3 \cdot 9\text{H}_2\text{O}$  and 1.0000 g of  $\text{CO}(\text{NH}_2)_2$  were added into 50 mL of deionized water. Then the mixture was completely dispersed via ultrasonic treatment at frequency of 45 kHz for 10 min. Thereafter, the mixture was transferred into a Teflon-lined stainless steel autoclave with 90 mL capacity. The autoclave was sealed and heated at 150 °C for 12 h and then cooled to room temperature naturally. The obtained product was washed by deionized water for 4 times and then dried at 70 °C for 6 h. Particularly, 0.8493 g of  $\text{AgNO}_3$  was introduced additionally during the synthesis of SPH–Ag material, with 1/2/2 loading mole ratio of Fe/P/Ag. In order to obtain single phase and well-crystallized of SPH–Ag, different preparation conditions, like mole ratio of Fe/P/Ag, reaction temperature, reaction time and pH (amount of urea), were optimized by a series of experiments.

### 2.2. Material characterization

X-ray diffraction (XRD) patterns were obtained on a RU-200 B rotation anode high power X-ray diffractometer (Rigaku, Japan). Transmission electron microscopy (TEM) was implemented on a JEM-2100F system (Hitachi, Japan). The morphologies of the samples were collected by a JSM-IT300 scanning electron microscopy (JEOL, Japan). The  $\text{N}_2$  sorption–desorption isotherm was measured by ASAP adsorption instrument (micromeritics, American). X-ray photoelectron spectroscopy (XPS) was performed on a K-Alpha XPS instrument (Thermo, American). The XPS valance band spectrum is corrected by Au and the obtained value is considered to be equivalent to the value vs NHE. UV-vis DRS spectra were measured on a UV2550 UV-vis spectrophotometer (Shimadzu, Japan) with  $\text{BaSO}_4$  as a reflectance standard. Photoluminescence (PL) emission spectra were collected on a RF-5301PC spectrofluorometer (Shimadzu, Japan) with emission wavelength of 320 nm. The Fourier transform-infrared spectroscopy (FT-IR) was measured by a NEXUS spectrometer (Thermo Nicolet, American) with scanning range of 10000–100  $\text{cm}^{-1}$ . The element

contents were determined by inductively coupled plasma-optical emission spectra (ICP) on a Prodigy 7 system (Leeman Labs, American). Photoelectro-chemical experiments were carried out on a CHI660E computer-controlled electrochemical workstation. The electronic spin resonance (ESR) signals for  $\cdot\text{O}_2^-$  radicals in the suspended photocatalysts with 0.2 mL of 50 mM 5,5-dimethyl-1-pyrroline N oxide (DMPO) was recorded on an A300-10/12 electron paramagnetic resonance spectrometer (Bruker, America) under visible light irradiation. TOC concentration was collected on a TOC-V CPH instrument (Shimadzu, Japan).

### 2.3. Photocatalytic measurement

In this work, the photocatalytic performances of the prepared samples were estimated by ARG degradation under visible light irradiation. ARG is a typical carcinogenic azo dye, which is widely utilized in the printing and dyeing industry. In a typical experiment, a dark adsorption experiment was carried out in advance. 0.5 g/L of catalyst and 100 mL of ARG solution (20 mg/L) was mixed in dark environment to achieve absorption–desorption equilibrium within 30 min. Afterwards, the mixture was exposed under a 300 W Dye lamp with 400 nm cut off filter. Meantime, 5 mL of ARG solution was collected over a certain time interval. UV-vis spectrophotometer (UV1750, Shimadzu Corporation, Japan) was used to measure the concentration of ARG solution.

## 3. Results and discussion

### 3.1. Structure and morphology properties of the samples

**Fig. 1** presented the  $2 \times 2 \times 2$  structure and the basic building unit of spheniscidite. The spheniscidite exhibits special three-dimensional open-framework consisted of  $\text{FeO}_6$  octahedra and  $\text{PO}_4$  tetrahedron. As shown in the basic building unit, two  $\text{FeO}_6$  octahedra share an edge delimited by two hydroxyl bonds which are also shared with other two satellite  $\text{FeO}_6$  octahedra, each of whose vertex is occupied by one water molecule. The  $\text{FeO}_6$  octahedra and  $\text{PO}_4$  tetrahedron are linked through sharing two or three corners, forming cylindrical tunnels which are occupied by free  $\text{NH}_4^+$  cations and  $\text{H}_2\text{O}$  molecules. As mentioned above,  $\text{NH}_4^+$  in tunnels can be exchanged by other cations like  $\text{K}^+$ . For better understanding of the spheniscidite structure,  $3 \times 3 \times 3$  structure of the spheniscidite showing along the [100], [010], [001] and [101] direction are shown in **Fig. S1**.

According to a series of synthesis experiments (Fig. S2 to Fig. S4 in Supplementary data), the typical SPH–Ag sample was obtained at 150 °C for 12 h by hydrothermal method, with 1/2/2 mol ratio of Fe/P/Ag and 1 g of urea content. **Fig. 2(a–c)** shows the XRD patterns and SEM images of the SPH and the typical SPH–Ag sample. As shown in **Fig. 2a**, the diffraction peaks of the SPH is in good agreement with the standard peaks of monoclinic spheniscidite (JCPDS 82-1164), which suggesting the formation of single phase spheniscidite material. After the

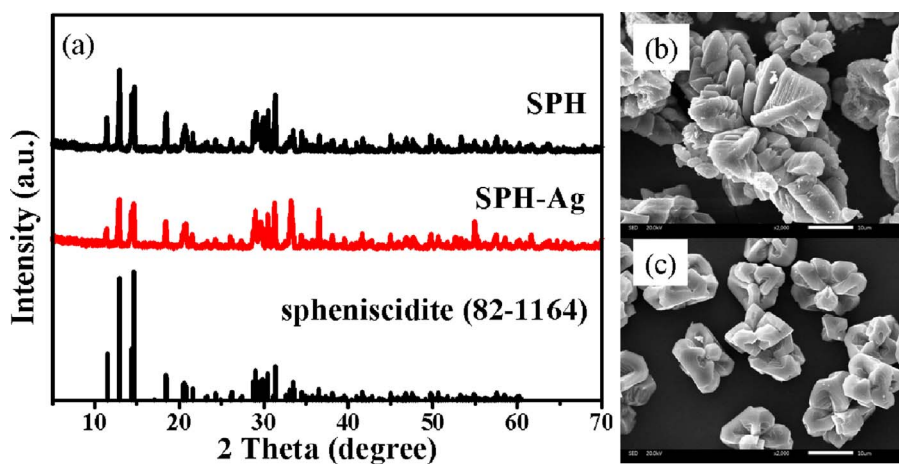


**Table 1**  
The calculated crystal structure parameters of SPH and SPH-Ag.

sample	lattice parameter (Å)				BET surface area (m <sup>2</sup> /g)
	<i>a</i>	<i>b</i>	<i>c</i>	<i>beta</i> (deg.)	
SPH	9.8169	9.7334	9.8664	102.7904	3.70
SPH-Ag	9.8291	9.7366	9.8689	102.8381	30.22

introduction of Ag source, no obvious change is observed in the XRD pattern of the SPH-Ag as compared to that of the SPH, indicating that Ag<sup>+</sup> has entered into the interconnected tunnels and took the place of NH<sub>4</sub><sup>+</sup> without destroying the monoclinic structure, which could be attributed to the similar radius and same valance state of NH<sub>4</sub><sup>+</sup> and Ag<sup>+</sup>. It is further confirmed by the similar cell parameters of the SPH and the SPH-Ag calculated from the obtained XRD patterns by Unit Cell software package, which is shown in Table 1. Besides, as SEM images (Fig. 2(b, c)) shows, the SPH-Ag exhibits uniform flower-like morphology, whose size is less than one-fifth of the SPH, indicating that Ag<sup>+</sup> effectively inhibited the further crystal growth of the SPH-Ag. Meanwhile, the specific surface area of the SPH-Ag (shown in Table 1) calculated by BET method from N<sub>2</sub> sorption desorption isotherm is 30.22 m<sup>2</sup>/g, which is 8 times higher than that (3.70 m<sup>2</sup>/g) of SPH. The higher surface area and smaller particle size of the SPH-Ag are beneficial for offering more active sites and better properties of transport and separation of electron–hole pairs.

Fig. 3(a) shows the microsized particle of the typical SPH-Ag sample. The Fe/P/Ag mole ratio of the SPH-Ag is calculated to be about 8/8/1 from ICP result (in Fig. 3(b)). Interestingly, the corresponding loading mole ratio of Fe/P/Ag is 1/2/2, which means only a small amount of Ag<sup>+</sup> successfully entered into the interconnected tunnels and replaced NH<sub>4</sub><sup>+</sup>. However, when the loading content of Ag<sup>+</sup> halved during the preparation process, the measured ratio of Fe/P/Ag is about 31/31/1. The results indicate that high loading concentration of Ag<sup>+</sup> is in demand so that enough Ag<sup>+</sup> would enter into the cavities and substitute NH<sub>4</sub><sup>+</sup>. On the other hand, excess Ag<sup>+</sup> would possibly destabilize the crystal structure of the SPH-Ag and result in the formation of Ag<sub>3</sub>PO<sub>4</sub> (shown in Fig. S4). The inference was further demonstrated by DFT calculation. The free energy values of the SPH unit cell structure with different amount of NH<sub>4</sub><sup>+</sup> substituted by Ag<sup>+</sup> were calculated by VASP package based on the first principle theory. The SPH unit cell structure without Ag<sup>+</sup> is shown in Fig. 4(a). According to the ICP result, the Fe/P/Ag ratio of the typical APH-Ag is 8/8/1, which means about one NH<sub>4</sub><sup>+</sup> was replaced by Ag<sup>+</sup> per unit cell (SPH-Ag-1, shown in Fig. 4(b)). For comparison, the free energy of SPH with two NH<sub>4</sub><sup>+</sup> substituted by Ag<sup>+</sup> (SPH-Ag-2, shown in Fig. 4(c)) was also calculated. (Note that the substituted amount of NH<sub>4</sub><sup>+</sup> in the SPH-Ag-2 is 1.5 per

unit cell since one of the NH<sub>4</sub><sup>+</sup> is shared by two unit cells.) As the calculated results showed in Fig. 4(d), when one Ag<sup>+</sup> replaced one NH<sub>4</sub><sup>+</sup> per unit cell, the free energy value of the monoclinic structure sharply decreases from -610.29 eV to -646.08 eV, indicating that the SPH-Ag-1 is much more stable than the SPH. While the free energy value of the SPH-Ag-2 dramatically increases to -570.67 eV, which means the extra replacement of NH<sub>4</sub><sup>+</sup> by Ag<sup>+</sup> would possibly destroy the balance of spheniscidite structure. Thus, moderate amount of Ag<sup>+</sup> would take the place of NH<sub>4</sub><sup>+</sup> and make the crystal structure more stable.

Fig. 3(c) illustrates the FT-IR spectra of the SPH and the SPH-Ag. The characteristic bands at 3477 cm<sup>-1</sup> (3478 cm<sup>-1</sup>) and 3342 cm<sup>-1</sup> are assigned to the stretching vibration of OH bonds on FeO<sub>6</sub> octahedra and the surface adsorbed water, respectively. The peaks at 2850–3040 cm<sup>-1</sup> are due to the H<sub>2</sub>O located in the tunnels and on the vertex of FeO<sub>6</sub> octahedra. Specifically, the peaks observed at 1645 cm<sup>-1</sup> and 1428 cm<sup>-1</sup> (1429 cm<sup>-1</sup>) are attributed to the v2 and v4 vibration of the relaxed NH<sub>4</sub><sup>+</sup> cation in the tunnels [32]. The peak of Fe–O from FeO<sub>6</sub> octahedra is observed at 547 cm<sup>-1</sup> (548 cm<sup>-1</sup>). The bands located at 980–1100 cm<sup>-1</sup> and 410–630 cm<sup>-1</sup> are ascribed to the asymmetric stretching and asymmetric bending vibration of PO<sub>4</sub> tetrahedron, respectively [33]. As the result shows that no new surface chemical bond occurred after the introduction of Ag<sup>+</sup>, excluding the existence of Ag-contained chemical bonds on the material surface.

The UV-vis DRS spectra of the SPH and the SPH-Ag are displayed in Fig. 3(d). Both the SPH and the SPH-Ag show positive response to visible light. Specifically, the absorption edge of the SPH is estimated to be about 420 nm, while the absorption edge of the SPH-Ag significantly red-shifted to 485 nm. Moreover, the visible light absorption of the SPH-Ag in the range of 350–700 nm is greatly enhanced as compared to that of the SPH. The embossment occurred at wavelength of 410–450 nm was considered to arise from the oxygen vacancy defects [34] in the SPH and SPH-Ag structures (Fig. S5). The optimized optical property of the SPH-Ag could possibly be attributed to Ag<sup>+</sup> modification. The optical band gaps of the SPH and the SPH-Ag are estimated by the following equation.

$$(ahv)^n = k(hv - E_g)$$

where *a*, *hν*, *k*, *E<sub>g</sub>*, *n* are the absorption coefficient, optical frequency, material constant, optical band gap and characteristic value of the transition, respectively. The *n* is 2 for direct allowed transition semiconductors and 0.5 for indirect allowed transition semiconductors. The electron transition type of the SPH and SPH-Ag were determined to be direct allowed and indirect allowed transition respectively via DFT calculation proceeded on VASP package (illustrated in Fig. S6). According to the Tauc plot shown in the inset of Fig. 3(d), the band gap values of the SPH and the SPH-Ag are estimated to be 3.0 eV and

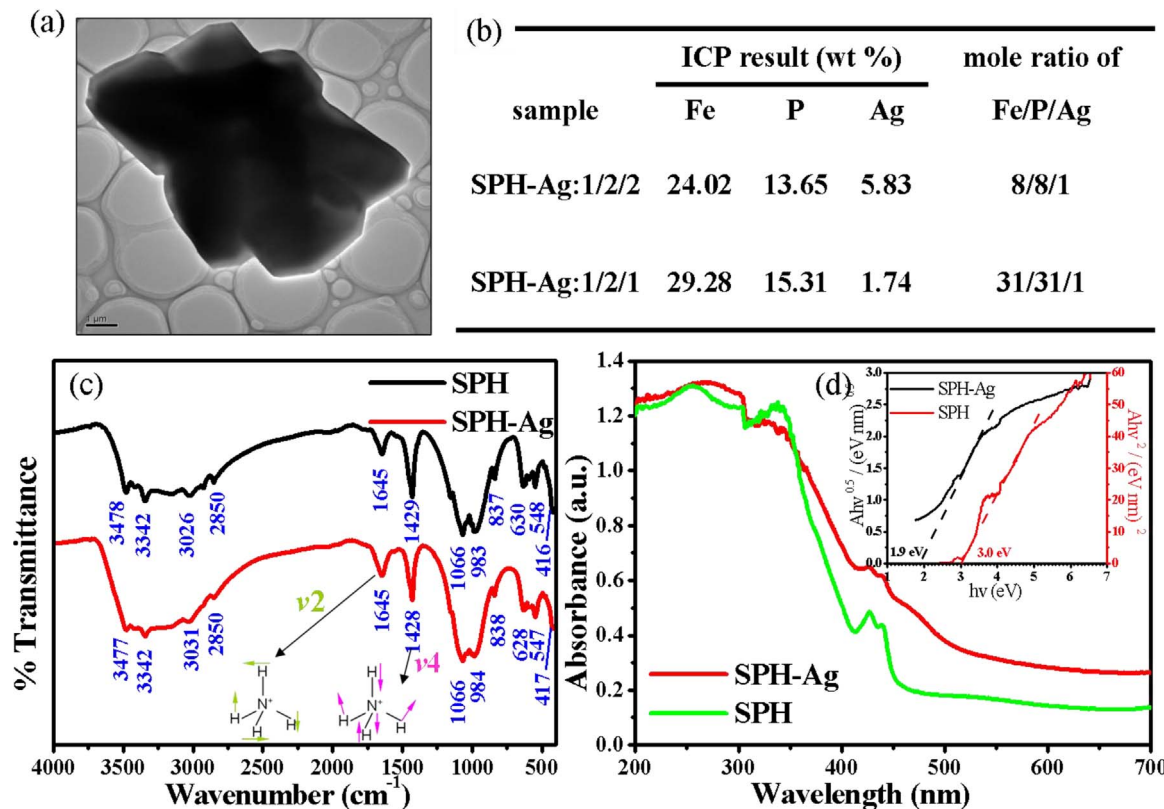


Fig. 3. (a) TEM images of SPH–Ag, (b) ICP result of SPH–Ag with different dosage of Ag, (c) FT-IR spectra and (d) UV-vis DRS spectra of SPH and SPH–Ag.

1.9 eV, respectively. Therefore,  $\text{Ag}^+$  introduction greatly decreased the band gap value of SPH and the SPH–Ag is more favorable to be motivated by visible light.

The chemical composition of the SPH and the SPH–Ag is determined by XPS spectra. As shown in Fig. 5(a), binding energy peaks of Fe, P, O, N and C can be clearly observed in the XPS survey scan of the SPH and the SPH–Ag, while C element is possibly due to the carbon source in XPS instrument and environment. Noticeably, the Ag 3d peaks present in the XPS spectra of the SPH–Ag. To further reveal the element chemical state, the high resolution XPS spectra are presented in Fig. 5(b, c). As for Fe 2p spectrum of the SPH, the bands at 712.20 eV and 725.90 eV are ascribed to  $\text{Fe} 2\text{p}_{3/2}$  and  $\text{Fe} 2\text{p}_{1/2}$  peaks, together with the satellite

peak at 718.22 eV, demonstrating the existence of  $\text{Fe}^{3+}$  species in the SPH. Similarly, the Fe chemical state in the SPH–Ag is also decided to be  $\text{Fe}^{3+}$ . Noteworthy, the Fe 2p<sub>1/2</sub> peak in the XPS spectrum of the SPH–Ag showed an obvious blue shift to the binding energy of 725.40 eV, suggesting the enhancement of electron density around Fe atom after Ag introduction. The XPS result is accordance with the electron localization functions of the SPH and SPH–Ag materials (shown in Fig. 6). This phenomenon could be attributed to the orbital hybridization between Fe and Ag atoms, which strengthening the interaction of Fe and Ag and reinforcing the stable existence of Ag in the cavities. Similar phenomena could be observed in the O 1s spectra of the SPH and SPH–Ag (Fig. S5). For Ag 3d spectrum of the SPH–Ag

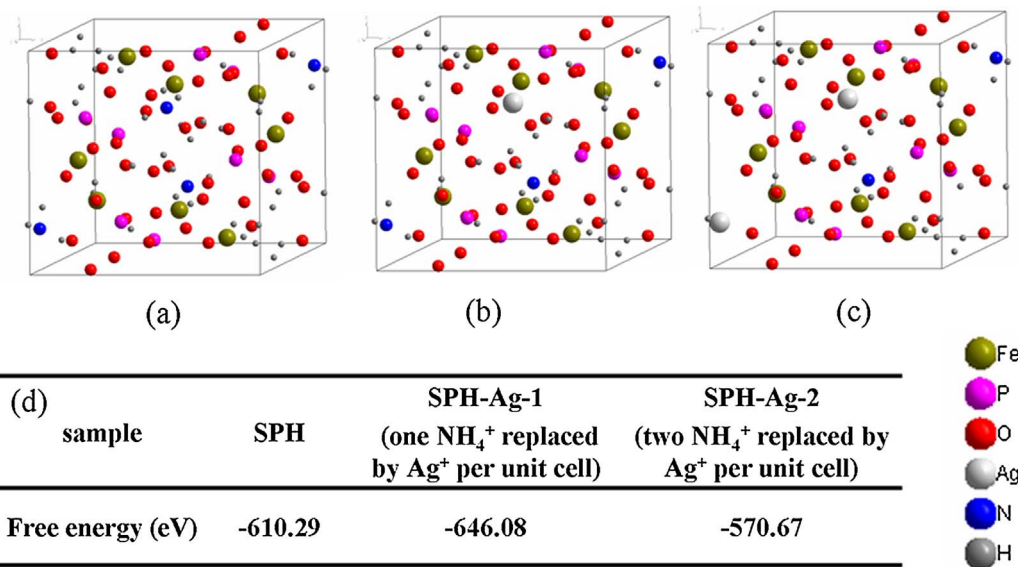


Fig. 4. The unit cell structure of (a) SPH, (b) SPH–Ag–1 and (c) SPH–Ag–2, together with (d) its corresponding free energy calculated by VASP package.

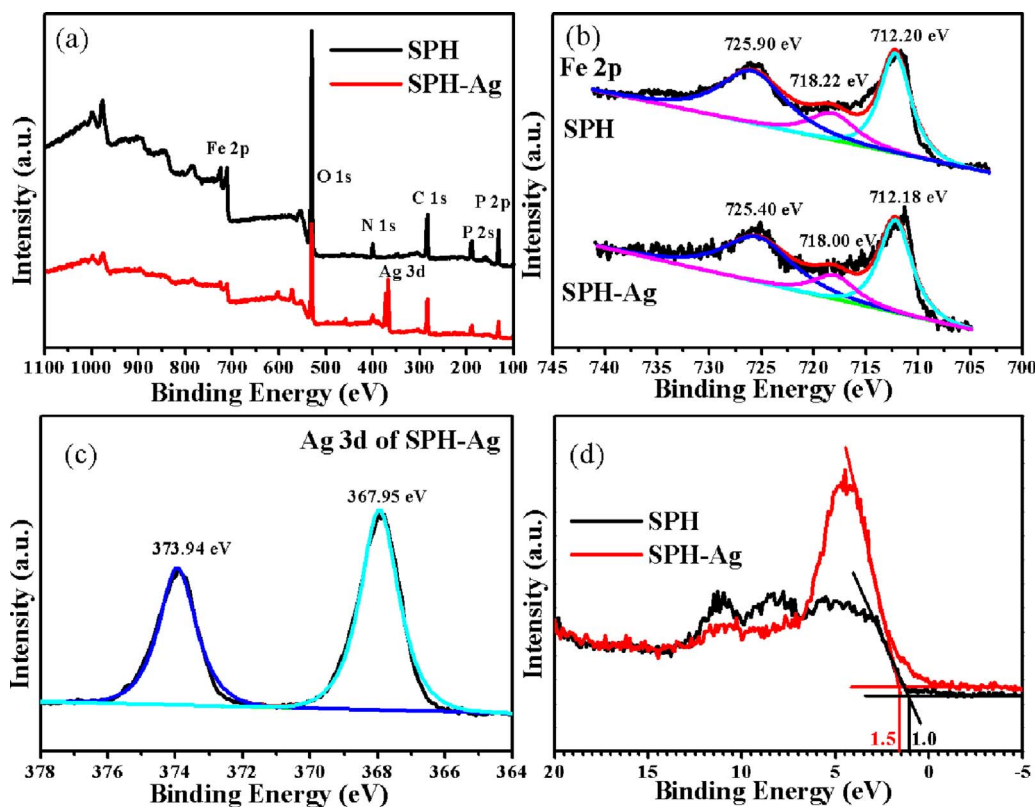


Fig. 5. (a) XPS survey spectra of SPH and SPH-Ag, and their corresponding high resolution XPS spectra of (b) Fe 2p, (c) Ag 3d and (d) valence band spectra.

catalyst, the peaks centered at 367.95 eV and 373.94 eV can be identified as  $\text{Ag}^+$  in the SPH-Ag cavities [35,36]. The XPS results exclude the existence of  $\text{Ag}^0$  in the SPH-Ag material. On the basis of the above XPS results, Fe, Ag and O atoms in the SPH-Ag structure had strong orbital hybridization, which enabled  $\text{Ag}^+$  to exist in the channels steadily. The inference is demonstrated by DFT calculation hereinafter. The valence band XPS spectra of the SPH and SPH-Ag catalysts were also carried out to evaluate the valence band edge position, which is shown in Fig. 4(d). The valence band of the SPH and SPH-Ag is estimated to be 1.0 V vs NHE and 1.5 V vs NHE, respectively. Associated with the obtained band gap values, the conductive band of the SPH and SPH-Ag materials is calculated to be  $-2.0$  V vs NHE and  $-0.4$  V vs NHE, respectively. Based on the above results, the introduction of  $\text{Ag}^+$  greatly improves the electron accepting ability of the SPH-Ag material.

### 3.2. Photocatalytic activity evaluation

The photocatalytic activities of the obtained materials were estimated with ARG solution under visible light irradiation. As shown in Fig. 7(a), ARG is self-nondegradable under visible light irradiation. The SPH catalyst did not exhibit activity for ARG degradation possibly due to its broad band gap, big particle size, poor surface area and high recombination rate of electrons and holes. Meanwhile, the  $\text{Ag}^+$  modified SPH-Ag sample performed enhanced photocatalytic activity under visible light irradiation. More than 90% of ARG was degraded within 3 h. The UV-vis adsorption spectra of ARG presented in Fig. 7(b) rapidly weaken to total smoothness, which further determined the successful removal of ARG by the SPH-Ag material. As shown in Fig. S7, the TOC concentration of ARG solution during the reaction process decreased from 8.4 mg/L to 4.1 mg/L, indicating that partial ARG was successfully mineralized. Thus, the silver cation introduced into the SPH structure was proved to be favorable for the enhancement of its

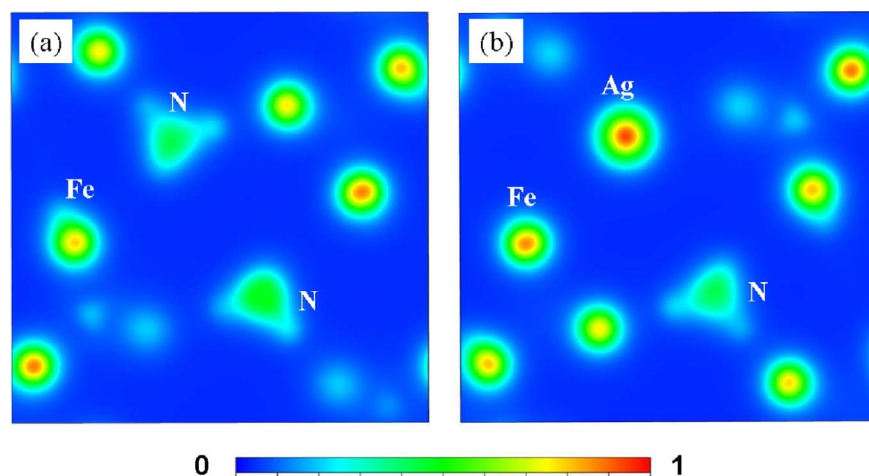


Fig. 6. Electron localization functions of the (a) SPH and (b) SPH-Ag photocatalysts.

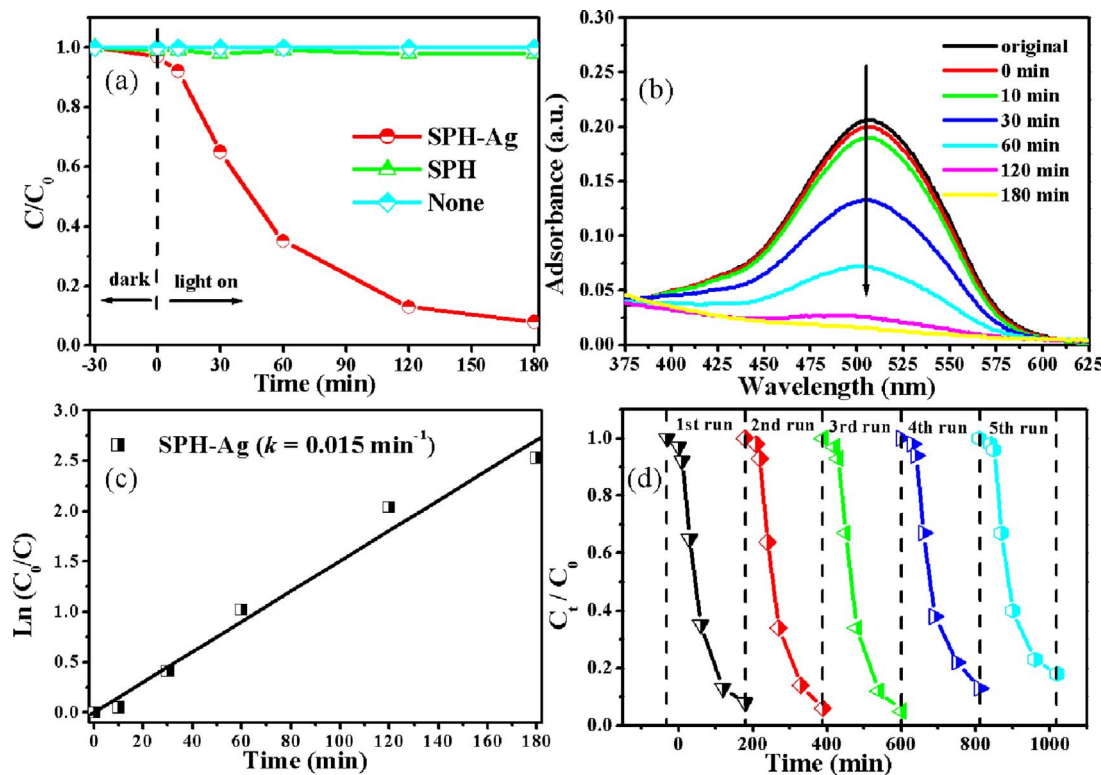


Fig. 7. (a) ARG degradation dynamics curves over different catalysts under visible light irradiation, (b) time dependent UV-vis absorption spectra of ARG solution over the SPH-Ag, (c) ARG degradation kinetic curve over the SPH-Ag and (d) stability measurement over the SPH-Ag.

photocatalytic activity. In addition, the ARG degradation kinetic properties with the presence of the SPH-Ag was investigated by the pseudo first-order kinetic model  $\ln(C_0/C) = kt$  [37], where  $C_0$ ,  $C$ ,  $t$  and  $k$  are respectively the initial ARG solution, measured ARG concentration, reaction time and the first-order kinetic rate constant. As illustrated in Fig. 7(c), the kinetic rate over the SPH-Ag catalyst is  $0.015 \text{ min}^{-1}$ .

The stability of structure and photocatalytic activity to an ideal photocatalytic material is very essential. We carried out recycle experiments to evaluate the stability of the SPH-Ag catalyst, and the result is shown in Fig. 7(d). The used catalyst was collected by centrifugation and was dried at  $70^\circ\text{C}$  for 6 h without any other treatment. The ARG decomposition rates over the SPH-Ag were 92%, 94%, 95%, 87% and 82% at each ordinal recycle experiment, respectively. The visible light photocatalytic activity of the SPH-Ag material was maintained well after five recycles. The slight decrease of photocatalytic property during the last two recycles is mainly due to the mass loss in the recovery progress. Moreover, the stabilities of structure and chemical state of the SPH-Ag were further estimated by XRD, FT-IR and XPS technologies. As shown in Fig. S8, the XRD patterns, FT-IR spectra and XPS spectra of the fresh SPH-Ag and the five-recycled SPH-Ag show no obvious difference. Noteworthy,  $\text{Ag}^+$  existed in the tunnels was stable and was not reduced to  $\text{Ag}^0$  even after five recycles. Therefore, the structural and performance stability of the SPH-Ag make it a promising visible light photocatalyst.

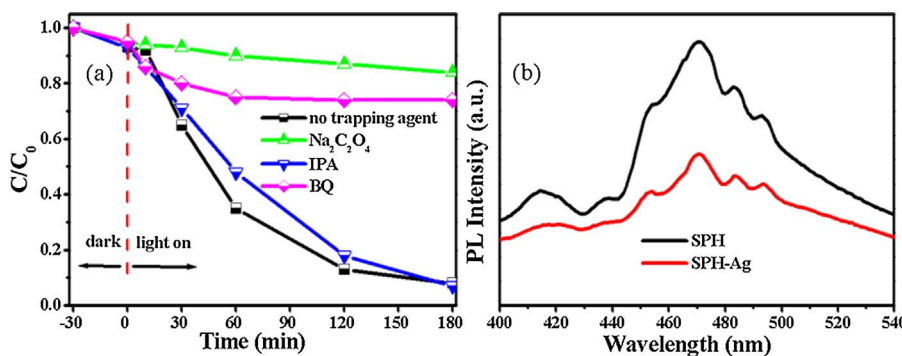
Generally, superoxide radical,  $\text{HO}^\cdot$  radical and hole are considered as the three major active radicals during the pollutant decomposition. As shown in Fig. 8(a), the trapping experiments were carried out with the addition of 2 mmol/L of isopropanol (IPA, a  $\text{HO}^\cdot$  scavenger), benzoquinone (BQ, a superoxide scavenger), or  $\text{Na}_2\text{C}_2\text{O}_4$  (a hole scavenger). About 93% of ARG solution was degraded by the SPH-Ag catalyst with the presence of IPA, indicating that  $\text{HO}^\cdot$  had no effect in it. On the opposite, the ARG removal rate sharply decreased from 92% to 16% and 26% respectively since  $\text{Na}_2\text{C}_2\text{O}_4$  and BQ were introduced

into the photocatalytic system. Therefore, hole and superoxide radical are determined to be the dominant active species in the ARG photodegradation process. To further confirm the existence of  $\cdot\text{O}_2^-$  radicals in the photocatalytic system, ESR test was carried out. As shown in Fig. S9, there is no ESR signal being observed in dark. However, the characteristic peaks of the DMPO- $\cdot\text{O}_2^-$  adducts occurred after 5 min of visible light irradiation, demonstrating the generation of  $\cdot\text{O}_2^-$  radicals on the typical SPH-Ag sample.

PL spectrum is a traditional and useful technology for evaluating the separation efficiency of electrons and holes in semiconductors. Lower recombination rate of charge carriers would be in response to lower PL intensity. Fig. 8(b) depicts the PL spectra intensity difference of the SPH and SPH-Ag samples. The PL intensity of the SPH-Ag catalyst is obviously lower than that of the SPH, indicating the former one is equipped with better separation efficiency of photo-induced carriers. The mechanism of the enhanced electron-hole separation of  $\text{Ag}^+$  modified SPH-Ag would be further discussed below.

### 3.3. Mechanism of silver modification and photocatalytic degradation

As described above, the silver modified SPH-Ag catalyst showed enhanced photocatalytic activity under visible light irradiation. Therefore, it is highly necessary to further investigate the existence form of silver and its modification mechanism. The valence of silver in the SPH-Ag sample was determined to be  $\text{Ag}^+$  by XPS spectra. Associated with the XRD patterns,  $\text{Ag}^+$  was considered to replace a certain fraction of  $\text{NH}_4^+$  in the tunnels of the structure. The rationalization of the above inference was enumerated as follows. Firstly,  $\text{NH}_4^+$  has the potential of being substituted by other cations according to the previous reports [16,19]. Secondly, there is great potential for  $\text{Ag}^+$  replacing  $\text{NH}_4^+$  due to their same valence state and similar radius. The substitution of  $\text{NH}_4^+$  by  $\text{Ag}^+$  would not destroy the structure and chemical balance of spheniscidite. Thirdly, theoretical calculation results (shown in Fig. 4) demonstrated that the SPH-Ag crystal structure



with certain amounts of  $\text{NH}_4^+$  replaced by  $\text{Ag}^+$  showed better stability. Fourthly, the changeless FT-IR and XRD results both suggest that  $\text{Ag}^+$  entered into the crystal architecture rather than depositing on the crystal surface or forming other Ag-contained compounds. Fifthly, the Fe, Ag, and O atoms showed strong interaction, which had positive effect on the stable existence of Ag in the cavities. Finally, in order to exclude the formation possibility of surface  $\text{Ag}^+$  doped SPH, ARG degradation experiment was carried out with the addition of the SPH and  $\text{AgNO}_3$ . The recycled sample was collected and characterized by XPS spectra. The results are presented in Fig. S10. More than 90% of ARG solution was fast degraded by the  $\text{AgNO}_3$  and SPH mixture within 1 h. However, the collected sample after reaction turned grey and showed poor recycle performance (Fig. S10(a)). Moreover, the valance state of silver in the used catalyst was determined to be  $\text{Ag}^0$  according to the XPS spectrum (Fig. S10(b, c)). Therefore, all the above theoretical and experimental results further confirm that  $\text{Ag}^+$  entered into the cavities of spheniscidite structure and replaced a certain fraction of  $\text{NH}_4^+$ .

In order to fully understand the modification mechanism of silver over the photocatalytic activity of SPH, the density of states (DOS) of the SPH-Ag and the partial density of states (PDOS) of the atoms were investigated by DFT over VASP package. According to the results depicted in Fig. 9, the CB edge and the VB edge of the SPH-Ag are mainly constituted of Fe 3d, O 2p and Fe 3d, O 2p, Ag 5s orbitals, respectively.

Noteworthy, Fe 3d, O 2p and Ag 5s orbitals exhibit strong hybridization at the VB of 1.2–2.4 eV, which is beneficial for the transfer and separation enhancement of photo generated charge carriers. Besides, it would also strengthen the interaction of Fe, Ag and O, reinforcing the stable existence of Ag in the cavities. As shown in Fig. 10, the arc radius in the EIS (electrochemical impedance spectroscopy) Nyquist plot of the SPH-Ag is smaller than that of the SPH, which suggested that the SPH-Ag owns faster transfer of the charge carriers. Meanwhile, the photocurrent density of the SPH-Ag is much higher than that of the SPH, which further confirmed that the photogenerated charge carriers in the SPH-Ag were more effectively transferred and separated than that in the SPH. The result of photoelectro-chemical tests are accordance with the DFT calculation results. Associated with the above results, silver cation effectively modified the structure and photocatalytic property of spheniscidite through the following ways. Firstly, the band gap structure of the catalyst was modified by  $\text{Ag}^+$  to equip with narrower band gap for visible light motivation and more positive VB position to generate holes with higher oxidizing ability. Secondly, the outer valance shell of the introduced silver cation hybridized with those of Fe and O atoms, which rearranging the valance composition and enhancing the separation of electrons and holes (in accordance with the results of PL and photoelectro-chemical tests). Thirdly,  $\text{Ag}^+$  has positive effect on the growth inhibition, resulting in

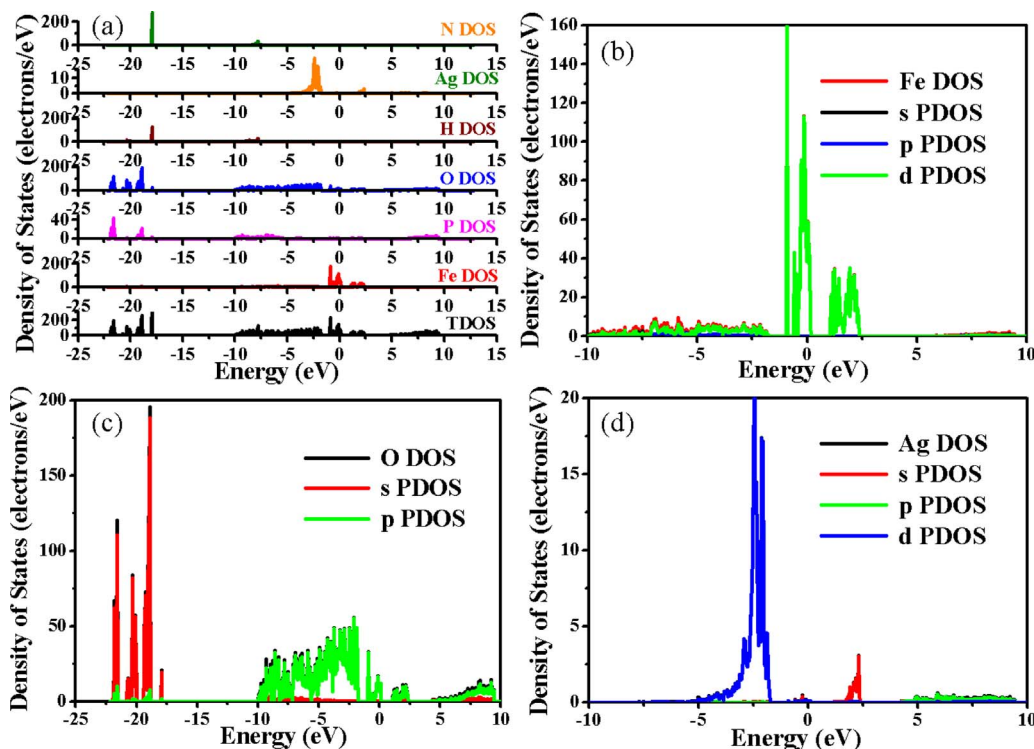


Fig. 9. (a) TDOS of SPH-Ag together with PDOS of (b) Fe atom, (c) O atom and (d) Ag atom.

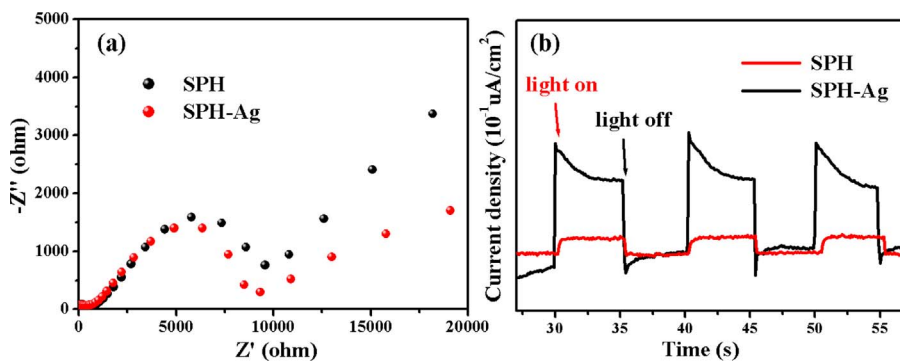


Fig. 10. EIS Nyquist plots (a) and photocurrent responses (b) of the SPH and typical SPH–Ag samples under visible light irradiation.

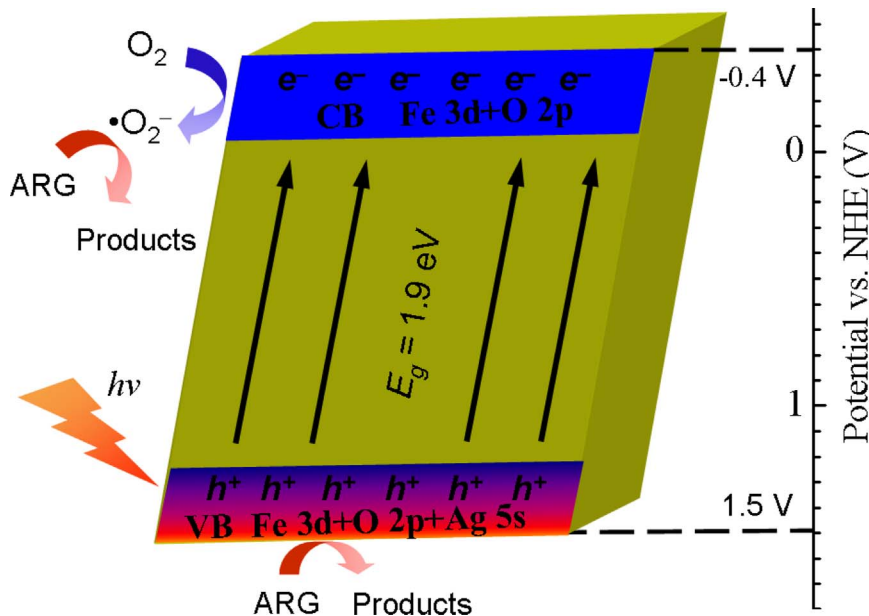


Fig. 11. The schematic mechanism of the ARG degradation over the SPH–Ag catalyst under visible light irradiation.

smaller particle size and larger surface area.

On the basis of the above results, the photodegradation mechanism of ARG over the SPH–Ag catalyst was proposed and illustrated in Fig. 11. The band gap energy ( $E_g$ ) of the SPH–Ag was estimated to be 1.9 eV, indicating it would be motivated by visible light to generate electrons and holes. The valence band (VB) of the SPH–Ag was measured to be 1.5 V vs NHE, while the conductive band (CB) was estimated to be  $-0.4$  V vs NHE. Since the photodegradation experiment was carried out at pH of about 7 and the CB position of the SPH–Ag is more negative than the standard potential of  $O_2/\cdot O_2^-$  ( $-0.33$  V vs NHE at pH = 7) [38], the photo generated electrons on the CB of the SPH–Ag would react with  $O_2$  to yield superoxide radicals. On the other hand, the VB position of the SPH–Ag is more positive than the potential of  $H_2O/HO\cdot$  (2.29 V vs NHE at pH = 7) [38,39], resulting in the unavailable formation of  $HO\cdot$  by the reaction between  $H_2O$  and  $h^+$ . Hence, ARG in the solution was effectively decomposed by the  $\cdot O_2^-$  and  $h^+$  radicals, which was also verified by the trapping experiment.

#### 4. Conclusion

The silver modified SPH–Ag was synthesized by one step hydrothermal method. The optimized SPH–Ag sample exhibited pure phase of monoclinic spheniscidite. Besides,  $Ag^+$  was considered to enter into the spheniscidite tunnels and substitute for a part of  $NH_4^+$ . The optimized substitution amount of  $NH_4^+$  by  $Ag^+$  was analyzed to be about 1/4 by theoretical calculation, which was accordant with the ICP result. The silver modified SPH–Ag sample showed enhanced photocatalytic activity for ARG degradation under visible light irradiation. Furthermore,

its photocatalytic property was highly maintained as well as its structure and surface chemical properties after being used for 5 times. The introduced  $Ag^+$  was found to play an important role to enhance the photocatalytic activity of the SPH–Ag through narrowing band gap, enlarging specific surface area and promoting charge carriers separation. Photo generated holes and  $\cdot O_2^-$  were dominant active radicals in the ARG photodegradation process. This work contributes to the fabrication of novel catalysts with enhanced visible light catalytic activity for environmental decontamination.

#### Acknowledgements

This work was supported by NSFC (No. 51472194), National Program on Key Basic Research Project of China (973 Program) 2013CB632402 and the NSF of Hubei Province (2016CFA078).

#### Appendix A. Supplementary data

Supplementary data associated with this article can be found, in the online version, at <http://dx.doi.org/10.1016/j.apcatb.2017.10.070>.

#### References

- [1] Y. Choi, M.S. Koo, A.D. Bokare, D.H. Kim, D.W. Bahnemann, W. Choi, Sequential process combination of photocatalytic oxidation and dark reduction for the removal of organic pollutants and Cr (VI) using  $Ag/TiO_2$ , Environ. Sci. Technol. 51 (2017) 3973–3981.
- [2] S. Weon, J. Choi, T. Park, W. Choi, Freestanding doubly open-ended  $TiO_2$  nanotubes for efficient photocatalytic degradation of volatile organic compounds, Appl.

Catal. B: Environ. 205 (2017) 386–392.

[3] X.G. Liu, G.J. Dong, S.P. Li, G.X. Lu, Y.P. Bi, Direct observation of charge separation on anatase  $\text{TiO}_2$  crystals with selectively etched {001} facets, J. Am. Chem. Soc. 138 (2016) 2917–2920.

[4] H.X. Li, Z.F. Bian, J. Zhu, Y.N. Huo, H. Li, Y.F. Lu, Mesoporous Au/ $\text{TiO}_2$  nanocomposites with enhanced photocatalytic activity, J. Am. Chem. Soc. 129 (2007) 4538–4539.

[5] G.S. Li, Z.C. Lian, W.C. Wang, D.Q. Zhang, H.X. Li, Nanotube–confinement induced size-controllable g-C<sub>3</sub>N<sub>4</sub> quantum dots modified single-crystalline  $\text{TiO}_2$  nanotube arrays for stable synergistic photoelectrocatalysis, Nano Energy 19 (2016) 446–454.

[6] F.H. Liu, J. Yu, G.Y. Tu, L. Qu, J.C. Xiao, Y.D. Liu, L.Z. Wang, J.Y. Lei, J.L. Zhang, Carbon nitride coupled Ti-SBA<sub>15</sub> catalyst for visible-light-driven photocatalytic reduction of Cr (VI) and the synergistic oxidation of phenol, Appl. Catal. B: Environ. 201 (2017) 1–11.

[7] Q.Z. Wang, J.J. He, Y.B. Shi, S.L. Zhang, T.J. Niu, H.D. She, Y.P. Bi, Designing non-noble/semiconductor Bi/BiVO<sub>4</sub> photoelectrode for the enhanced photoelectrochemical performance, Chem. Eng. J. 326 (2017) 411–418.

[8] T.J. Yan, J. Tian, W.F. Guan, Z. Qiao, W.J. Li, J.M. You, B.B. Huang, Ultra-low loading of Ag<sub>3</sub>PO<sub>4</sub> on hierarchical In<sub>2</sub>S<sub>3</sub> microspheres to improve the photocatalytic performance: the cocatalytic effect of Ag and Ag<sub>3</sub>PO<sub>4</sub>, Appl. Catal. B: Environ. 202 (2017) 84–94.

[9] J. Li, L.J. Cai, J. Shang, Y. Yu, L.Z. Zhang, Giant enhancement of internal electric field boosting bulk charge separation for photocatalysis, Adv. Mater. 28 (2016) 4059–4064.

[10] Y.Y. Zhu, Q. Ling, Y.F. Liu, H. Wang, Y.F. Zhu, Photocatalytic performance of BiPO<sub>4</sub> nanorods adjusted via defects, Appl. Catal. B: Environ. 187 (2016) 204–211.

[11] Y.Y. Zhu, Y.J. Wang, Q. Ling, Y.F. Zhu, Enhancement of full-spectrum photocatalytic activity over BiPO<sub>4</sub>/Bi<sub>2</sub>WO<sub>6</sub> composites, Appl. Catal. B: Environ. 200 (2017) 222–229.

[12] S.Y. Bao, Z.Q. Wang, X.Q. Gong, C.Y. Zeng, Q.F. Wu, B.Z. Tian, J.L. Zhang, AgBr tetradecahedrons with co-exposed {100} and {111} facets: simple fabrication and enhancing spatial charge separation using facet heterojunctions, J. Mater. Chem. A 4 (2016) 18570–18577.

[13] B.C. Qiu, Q.H. Zhu, M.M. Du, L.G. Fan, M.Y. Xing, J.L. Zhang, Efficient solar light harvesting CdS/Co<sub>9</sub>S<sub>8</sub> hollow cubes for Z-Scheme photocatalytic water splitting, Angew. Chem. Int. Ed. 56 (2017) 2684–2688.

[14] J. Li, X.Y. Wu, W.F. Pan, G.K. Zhang, H. Chen, Vacancy-rich monolayer BiO<sub>2-x</sub> as highly efficient UV, visible and near-infrared responsive photocatalyst, Angew. Chem. Int. Ed. (2017), <http://dx.doi.org/10.1002/anie.201708709>.

[15] A. Choudhury, S. Natarajan, A synthetic iron phosphate mineral spheniscidite,  $[\text{NH}_4]^+[\text{Fe}_2(\text{OH})(\text{H}_2\text{O})(\text{PO}_4)_2]^- \cdot \text{H}_2\text{O}$ , exhibiting reversible dehydration, J. Chem. Sci. 111 (1999) 627–637.

[16] M.J. Wilson, D.C. Bain, Spheniscidite, a new phosphate mineral from elephant island, british antarctic territory, Mineral. Mag. 50 (1986) 291–293.

[17] M. Cavellec, D. Riou, G. Férey, Synthetic spheniscidite, Acta Cryst. 50 (1994) 1379–1381.

[18] A.C. Cheetham, G. Férey, T. Loiseau, Open-framework inorganic materials, Angew. Chem. Int. Ed. 38 (1999) 3268–3292.

[19] K.V. Redrup, M.T. Weller, Synthesis and crystal structures of iron hydrogen phosphates, Dalton Trans. (2009) 3786–3792.

[20] H. Zhou, H.B. Duan, H. Zhang, X.M. Ren, A new pseudo-polymorph in mineral spheniscidite family  $[\text{NH}_4][\text{Fe}_2(\text{OH})(\text{H}_2\text{O})(\text{PO}_4)_2] \cdot 1.5\text{H}_2\text{O}$  exhibiting spontaneous magnetization below 25 K, Solid State Sci. 12 (2010) 1816–1821.

[21] P. Reale, B. Scrosati, Synthesis and thermal behavior of crystalline hydrated iron (III) phosphates of interest as positive electrodes in Li batteries, Chem. Mater. 15 (2003) 5051–5058.

[22] Z.G. Yi, J.H. Ye, N. Kikugawa, T. Kako, S.X. Ouyang, H. Stuart-Williams, H. Yang, J.Y. Cao, W.J. Luo, Z.S. Li, Y. Liu, R.L. Withers, An orthophosphate semiconductor with photooxidation properties under visible-light irradiation, Nat. Mater. 9 (2010) 559–564.

[23] D.Y. Yoon, E.H. Lim, Y.J. Kim, J.H. Kim, T. Ryu, S. Lee, B.K. Cho, I.S. Nam, J.W. Choung, S. Yoo, NO oxidation activity of Ag-doped perovskite catalysts, J. Catal. 319 (2014) 182–193.

[24] M.K. Kim, P.S. Kim, J.H. Baik, I.S. Nam, B.K. Cho, S.H. Oh, DeNOx performance of Ag/Al<sub>2</sub>O<sub>3</sub> catalyst using simulated diesel fuel/ethanol mixture as reductant, Appl. Catal. B: Environ. 105 (2011) 1–14.

[25] P. Wang, B.B. Huang, X.Y. Qin, X.Y. Zhang, Y. Dai, J.Y. Wei, M.H. Whangbo, Ag@AgCl: a highly efficient and stable photocatalyst active under visible light, Angew. Chem. Int. Ed. 47 (2008) 7931–7933.

[26] H.F. Cheng, K. Fukui, Y. Kuwahara, K. Mori, H. Yamashita, Harnessing single-active plasmonic nanostructures for enhanced photocatalysis under visible light, J. Mater. Chem. A 3 (2015) 5244–5258.

[27] P. Verma, Y. Kuwahara, K. Mori, H. Yamashita, Pd/Ag and Pd/Au bimetallic nanocatalysts on mesoporous silica for plasmon-mediated enhanced catalytic activity under visible light irradiation, J. Mater. Chem. A 4 (2016) 10142–10150.

[28] J.D. Li, W. Fang, C.L. Yu, W.Q. Zhou, L.H. Zhu, Y. Xie, Ag-based semiconductor photocatalysts in environmental purification, Appl. Surf. Sci. 358 (2015) 46–56.

[29] H.J. Dong, G. Chen, J.X. Sun, Y.J. Feng, C.M. Li, C.D. Lv, Stability, durability and regeneration ability of a novel Ag-based photocatalyst, Ag<sub>2</sub>Nb<sub>4</sub>O<sub>11</sub>, Chem. Commun. 50 (2014) 6596–6599.

[30] G.P. Li, Y.X. Wang, L.Q. Mao, Recent progress in highly efficient Ag-based visible-light photocatalysts, RSC Adv. 4 (2014) 53649–53661.

[31] X.L. Zhu, P. Wang, B.B. Huang, X.C. Ma, X.Y. Qin, X.Y. Zhang, Y. Dai, Synthesis of novel visible light response Ag<sub>10</sub>Si<sub>4</sub>O<sub>13</sub> photocatalyst, Appl. Catal. B: Environ. 199 (2016) 315–322.

[32] A. Huczyński, J. Janczak, J. Rutkowski, B. Brzezinski, Spectroscopic, crystallographic and theoretical studies of lasalocid complex with ammonia and benzylamine, Spectrochim. Acta A 125 (2014) 297–307.

[33] H. Yu, D.G. Deng, Y.Q. Li, S.Q. Xu, Y.Y. Li, C.P. Yu, Y.Y. Ding, H.W. Lu, H.Y. Yin, Q.L. Nie, Electronic structure and photoluminescence properties of yellow-emitting Ca<sub>10</sub>Na(PO<sub>4</sub>)<sub>7</sub>:Eu<sup>2+</sup> phosphor for white light-emitting diodes, J. Lumin. 143 (2013) 132–136.

[34] S. Park, H.J. Song, C.W. Lee, S.W. Hwang, I.S. Cho, Enhanced photocatalytic activity of ultrathin Ba<sub>5</sub>Nb<sub>4</sub>O<sub>15</sub> two-dimensional nanosheets, ACS Appl. Mater. Interfaces 7 (2015) 21860–21867.

[35] D.D. Tang, G.K. Zhang, Ultrasonic-assisted fabrication of cocoon-like Ag/AgFeO<sub>2</sub> nanocatalyst with excellent plasmon enhanced visible-light photocatalytic activity, Ultrason. Sonochem. 37 (2017) 208–215.

[36] D.D. Tang, G.K. Zhang, Fabrication of AgFeO<sub>2</sub>/g-C<sub>3</sub>N<sub>4</sub> nanocatalyst with enhanced and stable photocatalytic performance, Appl. Surf. Sci. 391 (2017) 415–422.

[37] J.L. Wang, Y. Lu, L.Z. Zhang, Highly efficient photocatalytic removal of sodium pentachlorophenate with Bi<sub>3</sub>O<sub>4</sub>Br under visible light, Appl. Catal. B: Environ. 136 (2013) 112–121.

[38] X. Li, J.G. Yu, M. Jaroniec, Hierarchical photocatalysts, Chem. Soc. Rev. 45 (2016) 2603–2636.

[39] Z. Wan, G.K. Zhang, X.Y. Wu, S. Yin, Novel visible-light-driven Z-scheme Bi<sub>12</sub>GeO<sub>20</sub>/g-C<sub>3</sub>N<sub>4</sub> photocatalyst: oxygen-induced pathway of organic pollutants degradation and proton assisted electron transfer mechanism of Cr(VI) reduction, Appl. Catal. B: Environ. 207 (2017) 17–26.